bioRxiv preprint doi: https://doi.org/10.1101/2023.11.29.569190; this version posted November 30, 2023. The copyright holder for this preprint (which was not certified by peer review) is the author/funder, who has granted bioRxiv a license to display the preprint in perpetuity. It is made available under aCC-BY-NC-ND 4.0 International license.

# Shared architectural patterns across the human cortical mantle predict visual representations and capture behavior across the lifespan

Xiayu Chen[1], Xingyu Liu[1], Patricia Maria Hoyos[2], Edan Daniel Hertz[2], Jewelia K. Yao[2], Zonglei Zhen[1,3*], Jesse Gomez[2,4]

1. Beijing Key Laboratory of Applied Experimental Psychology, Faculty of Psychology, Beijing Normal University, Beijing, China
2. Princeton Neuroscience Institute, Princeton University, Princeton, NJ, USA
3. State Key Laboratory of Cognitive Neuroscience and Learning & IDG/McGovern Institute for Brain Research, Beijing Normal University, Beijing, China
4. Psychology Department, Princeton University, Princeton, New Jersey, USA

*Correspondence address: Zonglei Zhen, Ph.D. (zhenzonglei@bnu.edu.cn), Faculty of Psychology, Beijing Normal University, Beijing, 100875, China.

## Abstract

The microstructure of cells within human cerebral cortex varies across the cortical ribbon, where changes in cytoarchitecture and myeloarchitecture are thought to endow each region of cortex with its unique function. While fine-scale relative to a cell, these population-level changes impact architectural properties of cortex measurable in vivo by noninvasive MRI, such as the thickness and myelin content of cortex. This raises the question of whether or not we can use these in vivo architectural measures to understand cortical organization, function, and development more broadly. Using human visual cortex as a test bed, we found two architectural gradients, which not only underlie its structural and functional organization, but additionally predict the presence of new visual field maps and capture the lifespan trajectory and its behavioral relevance. These findings provide a more general framework for understanding visual cortex, showing that architectural gradients are a measurable fingerprint of functional organization and ontogenetic routines in the human brain.

bioRxiv preprint doi: https://doi.org/10.1101/2023.11.29.569190; this version posted November 30, 2023. The copyright holder for this preprint (which was not certified by peer review) is the author/funder, who has granted bioRxiv a license to display the preprint in perpetuity. It is made available under aCC-BY-NC-ND 4.0 International license.

A fundamental goal of brain research is to elucidate the functional properties of the structural elements of the brain, at an appropriate organizational scale. Classical architectural brain maps including cytoarchitectonic[1,2] and myeloarchitectonic[3] maps, derived from postmortem brain sections, have revealed strong correspondence with the functional properties of the cerebral cortex[4,5]. Recent observations of spatial gradients in gene expression across human cortex[6,7], especially in genes controlling the shape and distribution of dendrites and myelin, also suggest that changes in large scale architectural properties necessitate functionally distinct zones[8]. However, these maps cannot be built for individual brains in vivo to capture individual differences, or the functional, behavioral or developmental relevance of these larger scale organizational principles. MRI technological advances have made it possible to map architectural correlates in human cortex in a noninvasive, and importantly individual-specific way, to test if the individual variation in functional organization across brains is reflected in the variation of architectural features of cortex[9–11]. In the case of visual cortex, general trend along the cardinal axis have been observed in architectural features such as myelination in adults[12] and infants[13] and cortical thinning[14], as well as functional properties of neurons such as receptive field size[15,16] and temporal sensitivity[17,18]. A model explicitly linking these architectural and functional variations across the cerebrum, one that can generalize to yet-mapped regions of cortex as well as explain behavior and dynamics across the lifespan, would be a steppingstone towards bridging structural and functional properties of the living human brain.

More explicitly, to what extent do individuals demonstrate shared architectural features of cortex and how might individual differences in these structural patterns across development or adulthood capture differences in brain function and behavior[11]? Answering such a question would require a large-scale, multimodal MRI dataset to appropriately capture the range in architectural variation at the level of the population. To that end, we combine three datasets from the Human Connectome Project (HCP) which together sample the human lifespan from 5 to 100 years of age[19–21], and ask if there are shared motifs in architectural features of cortex across individuals and development. Using visual cortex as a test bed, we focus first on the structural MRI of HCP young adults (HCP-YA, N=1070, 22-37 years old)[20,22]. Based on T1-weighted (T1w) and T2-weighted (T2w) images, we produce for each individual two distinct maps: a map of cortical thickness[23] and a map of the T1w/T2w signal ratio[24]. While the thickness map is thought to be attributable to the organization of neuronal, glial, and neuropil tissue[25–28], the ratio map is thought to be sensitive to intracortical density of myelin and neurite structure density[24,29]. Importantly, maps of cortical thickness had any variance explainable by curvature removed to account for known thickness differences between gyri and sulci. Leveraging the field's deep understanding of its functional organization relative to cortical folding[30–37], we focus here on visual cortex as a test bed to understand how variation in the structure of the cortical mantle relates to changes in function.

To extract the concurrent spatial changes of the two architectural measurements across individuals, the two maps from each hemisphere are concatenated across individuals to perform a spatial principal component analysis (PCA)[38,39] in which participants are features and cortical

bioRxiv preprint doi: https://doi.org/10.1101/2023.11.29.569190; this version posted November 30, 2023. The copyright holder for this preprint (which was not certified by peer review) is the author/funder, who has granted bioRxiv a license to display the preprint in perpetuity. It is made available under aCC-BY-NC-ND 4.0 International license.

vertices are samples. As a result, the concatenated maps were linearly decomposed into a collection of orthogonal principal components, consisting of spatial maps (i.e., scores) and individual weights (i.e., loading) in pairs. The former explains how the structural properties change across the cortical sheet on each component and the latter describes how individual maps contribute to each component (Fig. 1a). Because the resulting PCs are very similar for the two hemispheres (Extended Data Fig. 1), only data from the right hemisphere are presented here for clarity. The first two PCs (i.e., PC1 and PC2) describe over 50% of the architectural variance across the cortical sheet (Fig. 1b). The individual weights indicate that each PC relied on an integration of myelin content and cortical thickness at a given spatial location (Fig. 1c), rather than a single feature, suggesting that together these two architectural features capture a unique, holistic structural pattern of human cortex not visible through a single measure alone (Extended Data Fig. 2).

Both PC1 and PC2 maps form spatial gradients whose values change smoothly as one traverses the cortical surface (Fig. 1d). Specifically, gradient 1 (i.e., PC1 score), shows an increase in scores as one travels from the fundus of the calcarine sulcus either dorsally towards the intraparietal sulcus or ventrally into the anterior temporal lobe. Higher PC1 vertex values correspond to lower myelin content and a thicker cortical sheet. Gradient 2 (i.e., PC2 score), on the other hand, demonstrates alternating score patterns that fluctuate across cortex. Higher PC2 scores correspond to both higher myelin content and thickness. Gradient 2 scores seem to be broadly organized into four distinct zones, mirroring the visual cortex's division from early visual field maps[40] into the ventral, lateral, and dorsal processing streams of the visual cortex[41–44]. The processing stream borders delineated in Figure 1d, while anatomically defined, follow the ridge of positive weights in gradient 2. Quantitatively, the distribution of scores for gradient 1 shift across the four processing streams while the score distributions of gradient 2 are evenly sampled within each processing stream (i.e., zero-centered) (Fig. 1e). Furthermore, gradient 2 exhibits a higher spatial frequency in the distribution of its scores. That is, for a given pair of vertices separated by a short distance, gradient 2 tends to show a larger difference in score values compared to the more spatially homogenous gradient 1 (Fig. 1f). Collectively, these findings demonstrate that gradient 1 acts as a global gradient enveloping the entire visual cortex, while gradient 2 acts as a local gradient specific to individual visual streams.

To get a deeper understanding of the shape of these topographies, we produced simulated models using cortical geometry for the two spatial gradients. For gradient 1, the calcarine sulcus was used as the fiducial line, and vertices of the cortical surface were assigned values based on their minimal geodesic distance to the calcarine sulcus. This simple simulation was able to capture 57.1% of the explainable variance in the topography of gradient 1 (Fig. 1g, left). Gradient 2, which was more complicated in shape, could nonetheless be simulated using anchor points positioned at local minima within each visual processing stream (Fig. 1g, right), and vertices of the cortical surface were assigned values based on their minimal geodesic distance to these anchor points. This map of geometric distance also captured a sizeable portion of the

bioRxiv preprint doi: https://doi.org/10.1101/2023.11.29.569190; this version posted November 30, 2023. The copyright holder for this preprint (which was not certified by peer review) is the author/funder, who has granted bioRxiv a license to display the preprint in perpetuity. It is made available under aCC-BY-NC-ND 4.0 International license.

explainable variance within the gradient 2 map (17.7%, Fig 1g, right). These simulation results again highlight the global and local characteristics of the two gradients.

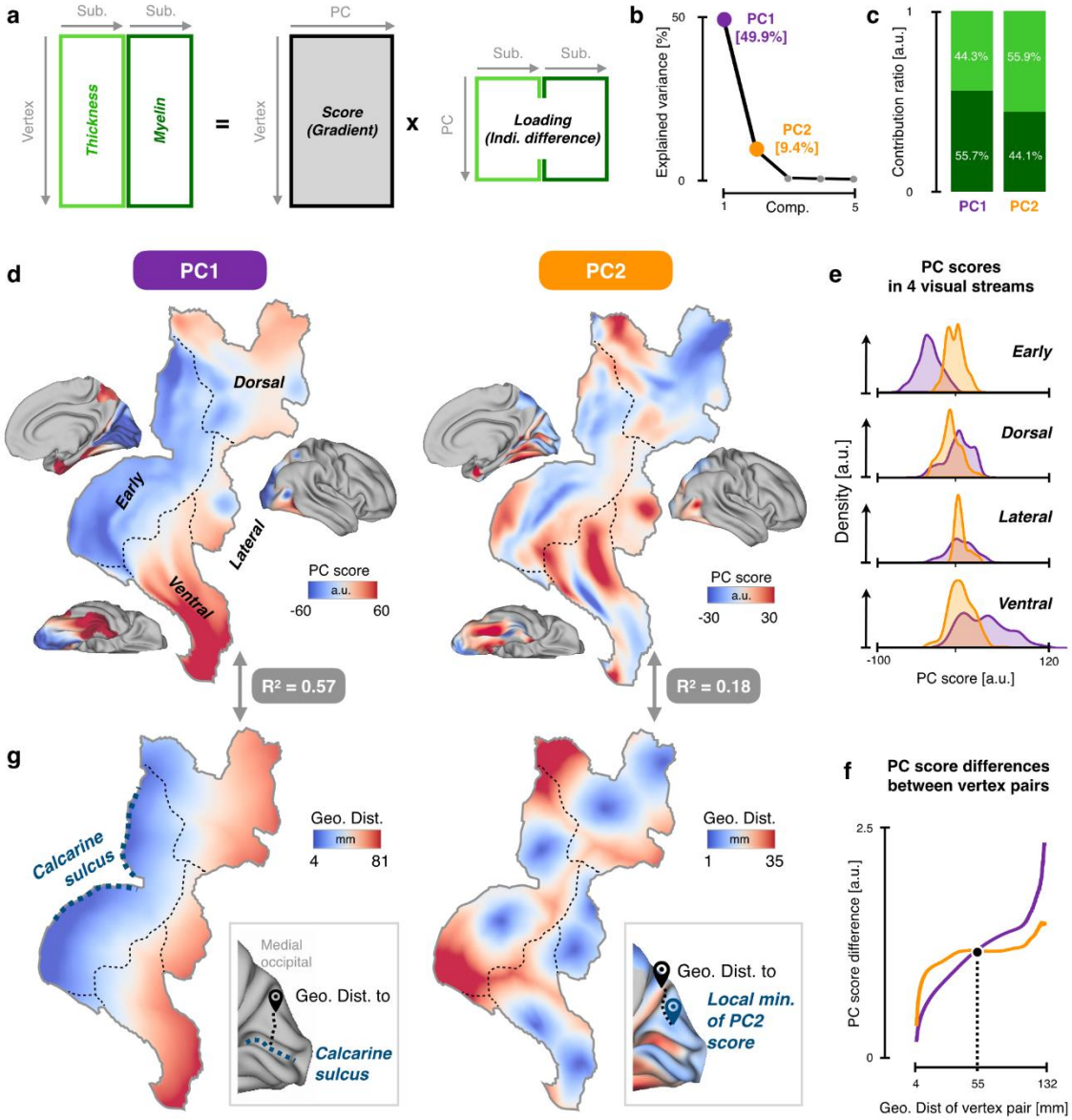


**Figure 1: Two architectural gradients scaffold human visual cortex. (a)** Principal component analysis (PCA) on the concatenated cortical thickness and myelin content maps from all participants in HCP-YA to extract architectural gradients of human visual cortex produced a collection of orthogonal principal components, consisting of spatial maps (i.e., score) and individual weights (i.e., loading) in pairs. **(b)** The explained variance ratio of the top 5 principal components (PCs). The first two PCs (i.e., gradients 1 and 2) dominate the explainable variance. **(c)** Contributions of the two architectural measures (thickness and myelin) to the two gradients. **(d)** Topographic patterns of the two gradients on a flattened cortical surface. Gradient 1 (PC1) displays roughly monotonic change from negative to positive scores across visual cortex, emanating from primary visual cortex V1, while gradient 2 (PC2) showed repeated representation in four localities, mirroring the four visual streams (early, dorsal, lateral, ventral). Black dotted lines: borders where the different visual streams meet, defined using HCP-MMP label boundaries. A.U. is arbitrary units. **(e)** Histogram depicting gradient scores in the four visual stream regions. Gradient 1 is a global gradient increasing from early to ventral, for example. Gradient 2 is a local gradient sampled evenly within individual visual stream. **(f)** The dependence of gradient value differences on geodesic distance are different for the two gradients. Gradient

bioRxiv preprint doi: https://doi.org/10.1101/2023.11.29.569190; this version posted November 30, 2023. The copyright holder for this preprint (which was not certified by peer review) is the author/funder, who has granted bioRxiv a license to display the preprint in perpetuity. It is made available under aCC-BY-NC-ND 4.0 International license.

1 shows larger changes across vertices separated by a long distance, whereas gradient 2 shows larger changes for short distances. **(g)** Geometric models of the two architectural gradients, which were constructed using the geodesic distance of each vertex of visual cortex to specific anatomical landmarks as anchors. The calcarine sulcus and eight local minima of gradient 2 were used as anchors to model gradient 1 and 2, respectively.

Do these architectural gradients reflect the functional organization of visual cortex? Given gradient 1 acts as a global gradient across the whole of visual cortex, we hypothesized that gradient 1 recapitulates the hierarchical organization of visual cortex and its constituent retinotopic maps. To test this, we examined the spatial similarity between the architectural gradients and the population receptive field (pRF) properties as measured by the HCP 7T retinotopy dataset[45]. The pRF represents the portion of visual space in which a stimulus evokes a response in a given voxel, and pRF size increases along the visual processing hierarchy[46–48]. We found that gradient 1 was highly correlated with the pRF size, while gradient 2 was not (Fig. 2a). Moreover, gradient 1 but not gradient 2 was perfectly correlated with the well-known hierarchical rank of the visual areas within the ventral stream (Fig. 2b). Thus, gradient 1 strongly captures the hierarchical organization of visual computations across cortex.

To provide further support for the hypothesis that gradient 1 might act as a broader-scale scaffold for functional properties of visual cortex, we can ask if it is also capable of describing temporal properties of functional activity. It is widely recognized that the brain shows a large-scale functional organization of the frequency at which the BOLD signal fluctuates during resting-state functional MRI[18,49,50]. This temporal property of the BOLD signal, quantified as a fractional value of low- versus full-frequency power (fALFF)[51], correlates well with temporal properties of receptive fields in visual cortex[17,18,52]. Here, we find that this temporal gradient as measured by fALFF is well-described by gradient 1 (Fig. 2c, right). In comparison, because gradient 2 acts as a local gradient, showing more spatial inhomogeneity with interdigitating peaks and valleys of scores within individual visual streams, we hypothesized that it might underlie the finer-scale division of visual cortex into distinct zones as a complement to gradient 1.

Along these lines, we tested if gradient 2 together with gradient 1, was capable of differentiating functional areas defined by the HCP multimodal parcellation[8]. As shown in the left part of Figure 2c, the combination of gradient 1 and gradient 2 greatly improved the predictive power of visual areas compared to using gradient 1 or gradient 2 alone. Moreover, as a separate validation of the hypothesis that gradient 2 scaffolds the fine arealization of visual cortex instead of global functional brain organization, we found gradient 2 adds little explanatory power on gradient 1 to a regression predicting fALFF values (Fig. 2c, right). Overall, both gradients seem to underlie distinct functional features of cortex: Gradient 1 recapitulates the hierarchical organization of visual cortex, while gradient 2 plays a potential role in fine areal differentiation of visual cortex. Strikingly, gradient 1 explains functional features of visual cortex (receptive field size, hierarchical rank) better than the first gradient derived from resting state functional connectivity (RSFC) within visual cortex (Extended Data Figure 3a-c). Additionally, the two architectural gradients outperform the first two RSFC gradients in classification of visual cortex into its constituent parcels (Extended Data Figure 3d). Lastly, if the two architectural

bioRxiv preprint doi: https://doi.org/10.1101/2023.11.29.569190; this version posted November 30, 2023. The copyright holder for this preprint (which was not certified by peer review) is the author/funder, who has granted bioRxiv a license to display the preprint in perpetuity. It is made available under aCC-BY-NC-ND 4.0 International license.

gradients truly relate to the functional organization of visual cortex in distinct ways, then these differences should be mirrored in the way cytoarchitecture contributes to each structural gradient. Based on the BigBrain dataset[53], we extracted cell body density data for each of the six cortical layers. For gradient 1, we find that changes in its structural features correlate strongly with cell density of layers III and IV, where the pronunciation of layer IV decreases with increasing distance from the calcarine sulcus. Gradient 2 was most correlated with cell density of layer I, with positive scores overlapping cortex with thicker superficial layers of cortex (Fig. 2d). Because the layers III and IV are primarily involved in feedforward connections whereas layer I majorly plays roles in feedback connections, the finding might suggest that the two gradients underlie structural fingerprints of feedforward and feedback processing in visual cortex, respectively.

Given the relatively tight correspondence between these architectural gradients and function properties of visual cortex, what can we learn about visual cortex organization more broadly, and more importantly, can this structural-functional coupling generalize to regions of visual cortex that have not yet been mapped? Upon examination of the topology of gradient 2, a pattern emerges between the gradient and retinotopic representations. While most of the anchor points for the gradient 2 map simulation correspond to visual field map clusters which share a foveal representation (V1-V4, VO1-2, IPS0-1, IPS2-3, TO1-2)[40,54], an additional anchor appeared in the anterior temporal lobe near the location where the occipitotemporal sulcus (OTS) merges with the collateral sulcus (CoS) more medially (Fig. 1g, right). If we assume a correspondence between gradient 2 anchors and visual field map clusters, then this anterior-most anchor would suggest an additional cluster of visual field maps in the anterior temporal lobe, one which has not yet been described in the literature. To test this hypothesis, and potentially demonstrate the predictive power of these architectural gradients to unmapped cortex, we performed pRF mapping[46] on 12 participants with high-contrast, socio-ecological images to better drive neurons of high-level visual cortex often tuned for such complex objects[55].

We indeed find a cluster of visual field maps in the anterior temporal lobe located medially overlapping the CoS and extending laterally towards the OTS usually just beyond the anterior tip of the fusiform gyrus but sometimes overlapping it (Fig. 2e). This location is consistent with a previous report of face-selectivity in the anterior temporal lobe[56]. These maps were observable in the majority of hemispheres (23/24 hemispheres; see Extended Data Fig. 4). This cluster of maps shows a clear radial representation of pRF eccentricity, with voxels near the center of the cluster sampling central visual space, and those near the outer boundary of the cluster sampling peripheral visual space. Perpendicular to this radial eccentricity representation was a representation of polar angle, with two upper visual field representations separated by a shared lower visual field representation, usually oriented at an oblique angle to the CoS but sometimes parallel with it (Fig. 2f). Consistent with spatial computations in earlier visual field maps, these anterior temporal maps, which we call here AT-1 and AT-2, have pRF centers that mainly sample the contralateral visual field[16,33,47], although it was not uncommon for pRF centers to sample ipsilateral visual space (Extended Data Fig. 4). Lastly, a hallmark feature of visual

bioRxiv preprint doi: https://doi.org/10.1101/2023.11.29.569190; this version posted November 30, 2023. The copyright holder for this preprint (which was not certified by peer review) is the author/funder, who has granted bioRxiv a license to display the preprint in perpetuity. It is made available under aCC-BY-NC-ND 4.0 International license.

pRFs is that they increase in size as one ascends the visual processing hierarchy, and the positive relationship between pRF eccentricity and size tends to become more dramatic as well[15,46–48]. To test this, we extract pRF fits from vertices with variance explained greater than 10%. We find that consistent with its high position within the processing hierarchy, pRF sizes are significantly larger than in earlier visual field maps V1 through V3, and the linear function relating pRF eccentricity and size yielded larger slopes compared to V1-V3 (Fig. 2g).

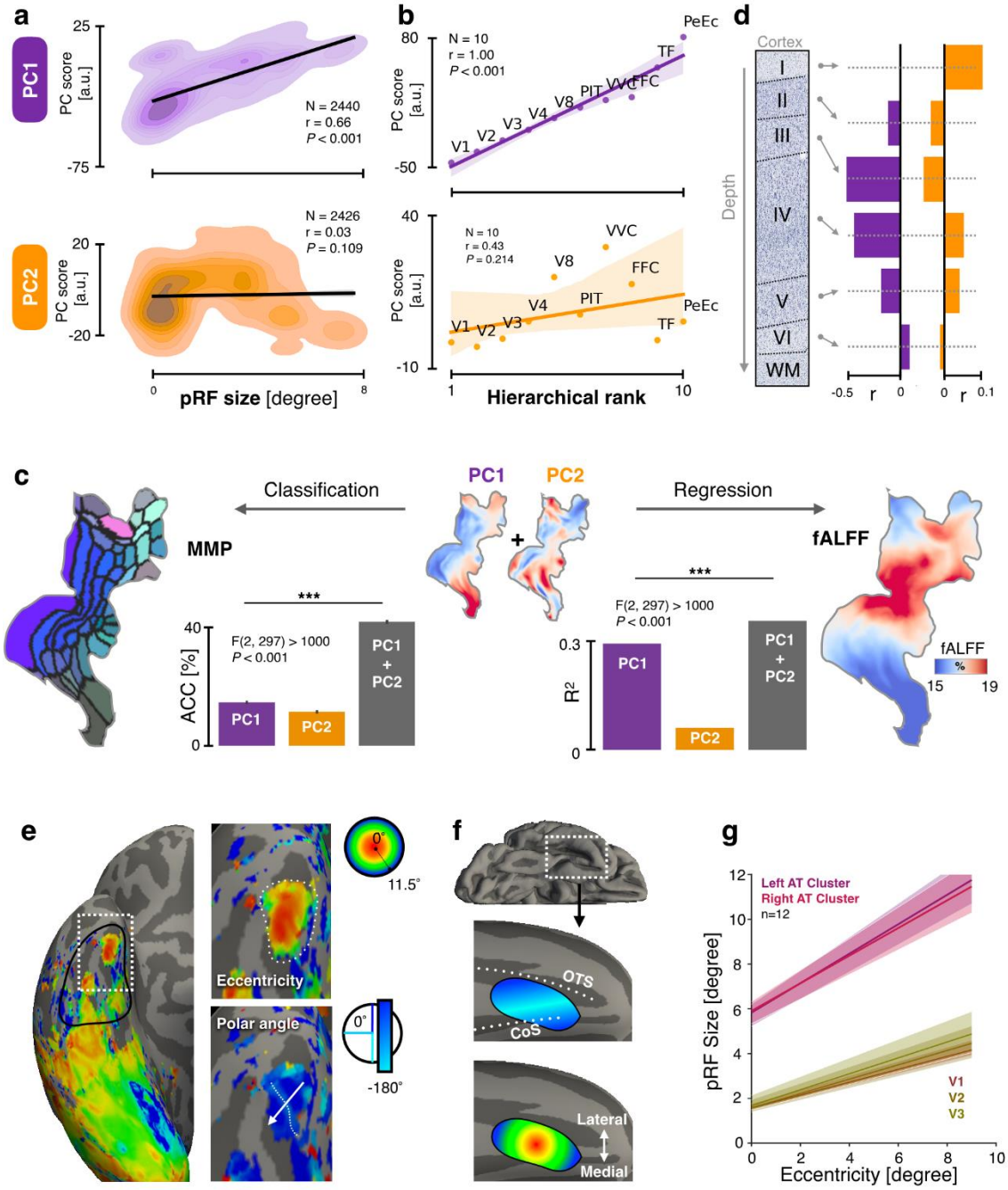


**Figure 2. The functional and microstructural properties of the two architectural gradients. (a)** Gradient 1 was highly correlated with the pRF size (r=0.66), while the gradient 2 was not (r=0.03). **(b)** Gradient 1 was perfectly correlated with the hierarchical rank of the 10 visual areas within the ventral visual stream (Spearman rank ρ=1.00), while gradient 2 was not. **(c)** The functional significance of the architectural gradients was

bioRxiv preprint doi: https://doi.org/10.1101/2023.11.29.569190; this version posted November 30, 2023. The copyright holder for this preprint (which was not certified by peer review) is the author/funder, who has granted bioRxiv a license to display the preprint in perpetuity. It is made available under aCC-BY-NC-ND 4.0 International license.

evaluated by measuring to what extent each gradient is related to areal differentiation of the visual cortex (left) and the global functional organization measured by fractional amplitude of low-frequency fluctuation (fALFF) from resting-state fMRI (right). The combination of gradients 1 and 2 greatly improved the predictive power of classifying visual areas compared to using either gradient alone. However, gradient 1 contributes more than gradient 2 in predicting the global-scale functional organization (i.e., fALFF map). **(d)** Cell body density from the BigBrain dataset is quantified for each cortical layer at each vertex and correlated with each gradient map. Gradient 1 was mainly correlated with cell body density in Layers III and IV, while gradient 2 was mainly correlated with cell body density in Layer I. **(e)** The architectural gradient 2 predicts the presence of novel visual field maps in the anterior temporal lobe. Left: example participant with the pRF eccentricity map displayed on the inflated cortical surface. The highlighted region (white dotted line) is the subject of the zoomed insets on the right. The black outline delineates the anatomical region from which pRF data was extracted. The putative visual field map cluster is outlined on the insets, showing a radial eccentricity representation, and a perpendicular representation of polar angle travelling roughly medio-anterior to latero-posterior as indicated by the white arrow. **(f)** Illustration on an inflated cortical surface illustrating that the AT-cluster of retinotopic maps is located near the anterior intersection of the occipitotemporal (OTS) and collateral sulci (CoS). The AT-cluster field maps demonstrate perpendicular representations of pRF eccentricity and polar angle. **(g)** In all 12 participants, pRF size and eccentricity from all above-threshold vertices within the anatomically-defined region (black solid line from panel e) are extracted, binned by eccentricity, averaged across participants, and then lines-of-best fit are modeled across the averaged data. Shaded regions represent bootstrapped 68% confidence intervals.

If these architectural gradients are capable of extrapolating to functional representations in broader visual cortex, to what extent can they also describe the behaviors supported by visual cortex? The PCA approach, in addition to providing spatial maps of scores, provides a weight or sense of fit describing how a given participant relates to a given gradient. To answer the question above, canonical correlation analysis (CCA)[57] was performed to examine how individual participant weights for the two gradients can predict the individual behavioral performance from 15 vision-related behavioral tasks[58] (Fig. 3a). As shown in Fig. 3b, both gradients show significant correlation with visual ability, with gradient 2 showing stronger correlation with the visual ability than gradient 1. Moreover, the two gradients are associated with distinct and unrelated behavioral profiles (Fig. 3c): Behavioral variables related to attention, visual acuity and inhibitory control contribute more to gradient 1, while vocabulary comprehension, fluid intelligence, spatial orientation processing ability, and nonverbal episodic memory ability contribute more to the gradient 2. The divergent mapping of each gradient onto distinct behaviors further underscores each architectural gradient's unique contribution to brain function. Overall, it seems that gradient 2 involves various complex visual processing abilities, while gradient 1 involves relatively primary and general visual processing functions.

If these architectural gradients across the cortical sheet correspond to differences in cortical tissue content, brain function, and behavior, as evidenced above, then they should also change across the lifespan, given that behavior and neocortical tissue structure develop dramatically during childhood across visual cortex[14,27,59]. The two spatial gradients described above were derived from the young adult dataset. We can therefore repeat the spatial component analysis at various stages of the lifespan, ask if the first two principal gradients replicate in these separate stages, and determine how they may change, if at all, across the lifespan using HCP development (HCP-D) and aging (HCP-A) datasets[60]. We binned participants in equal-sized

bioRxiv preprint doi: https://doi.org/10.1101/2023.11.29.569190; this version posted November 30, 2023. The copyright holder for this preprint (which was not certified by peer review) is the author/funder, who has granted bioRxiv a license to display the preprint in perpetuity. It is made available under aCC-BY-NC-ND 4.0 International license.

windows of increasing age, deriving within each window the top PCs and correlating their score maps with that from the young adult dataset. To distinguish the PCs of each age window from the PCs of the young adult dataset, we referred those derived from developmental age-bins as lifespan components (LC). We found that LC1 and LC2 from the developmental (n=652 participants, 351 females, ages 5-21), adult, and aging (n=725 participants, 406 females, ages 36-100) data at every age bin show a high correspondence to gradient 1 and gradient 2 from the young adult data respectively, compared to other LCs (Fig. 3d). This demonstrates that the two gradients derived from lifespan data at each window replicate those of the young adult dataset, allowing us to trace their developmental trajectories.

Examining the correlation between the young adult gradient and LC within each developmental window, we first found that LCs, as expected, are stable during young adulthood (Fig. 3e, middle). However, we found a linear change across childhood, with the topography of LC1 and LC2 becoming more adult-like with maturation (Fig. 3e, left). The trajectory of each LC was unique. LC2 showed a significantly larger developmental effect than LC1, with an annualized rate of change (AROC) four times that of LC1(0.86% vs. 0.20%). Finally, if gradients solidify their structural topography across childhood and adolescence, do they show degeneration in later adulthood? We can make two a priori hypotheses here: first, that both LCs will show linear loss of their adult-like topographies and second, that LC2 should show more rapid degeneration than LC1 potentially consistent with developmental "last-in-first-out" trends observed in white matter development[61]. The sliding-window gradient analysis on the aging dataset revealed that both hypotheses are supported, LC1 and LC2 both show linear loss of their topographies with LC2 (AROC: -0.17%) showing more dramatic degeneration than LC1 (AROC: -0.04%) (Fig. 3e, right).

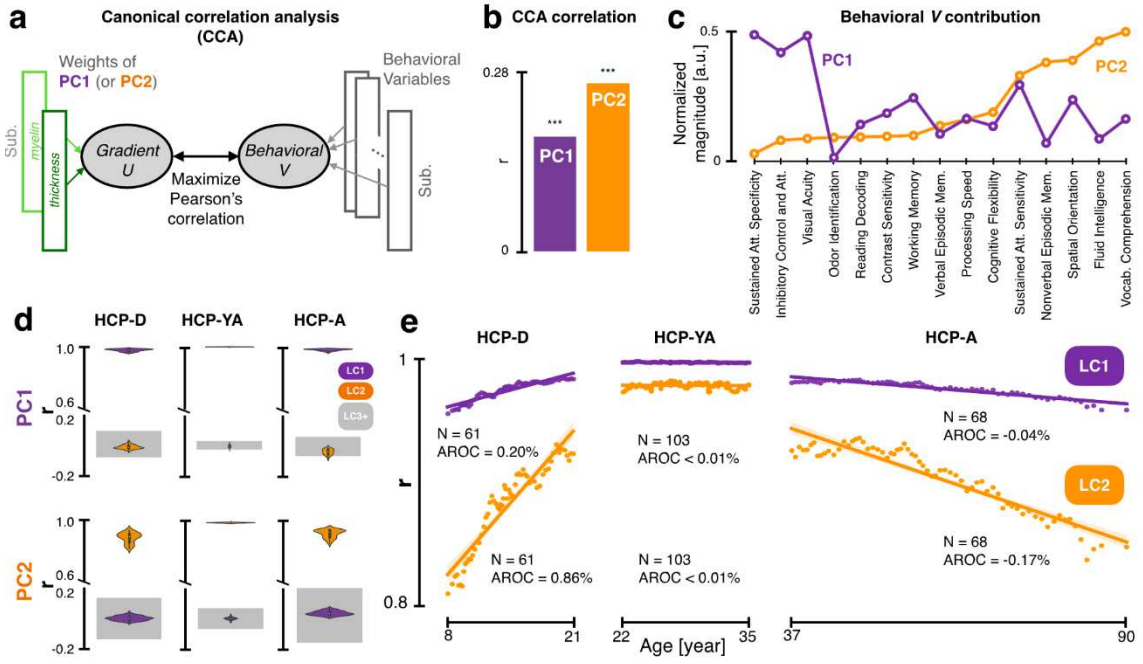


**Figure 3. The relevance of the architectural gradients to visual behavior, development, and degeneration across the lifespan. (a)** Canonical correlation analysis (CCA) was used to associate multiple vision-related

bioRxiv preprint doi: https://doi.org/10.1101/2023.11.29.569190; this version posted November 30, 2023. The copyright holder for this preprint (which was not certified by peer review) is the author/funder, who has granted bioRxiv a license to display the preprint in perpetuity. It is made available under aCC-BY-NC-ND 4.0 International license.

tasks with the two weight-vectors of each architectural gradient in the HCP-YA. CCA finds the linear combination of variables that best associate measures from the two data domains across participants. **(b)** Both architectural gradients can significantly predict individual visual ability. However, gradient 2 showed stronger correlation with visual behaviors than gradient 1. **(c)** The normalized magnitude of behavioral factor weights from CCA indicate that gradient 1 was correlated more with low-level visual abilities, while gradient 2 was correlated with higher-level visual abilities. **(d)** Sliding window spatial PCA was performed across the lifespan (PCA on a given age-bin results in "lifespan component", LC) to compare how the patterns of gradient 1 and 2 change with the age. The top two LCs (i.e., spatial maps) extracted from each age window correlate strongly with their respective component from the HCP Young Adult dataset, confirming that the architectural gradients can be observed across the lifespan. **(e)** Correlations between LCs and PCs reveal that gradient 2 shows more development and degeneration across childhood and aging, compared to gradient 1.

Overall, we provide evidence for mesoscale architectural gradients across human visual cortex wherein graded changes in both cortical thickness and myelin content scaffold cortex into a hierarchy of clustered cortical regions. The primary gradient ranges from thin high-myelin content cortex to thick low-myelin content, while the secondary ranges from cortical regions which are relatively thin and lightly-myelinated to thick and highly-myelinated. These two architectural gradients together describe well the broader functional landscape and seem to relate to unique aspects of cytoarchitecture across cortex. Where the first gradient correlates strongly with pRF size of the visual system, and is capable of ranking regions into their ground-truth hierarchical ordering, the second gradient not only predicted the location of a new cluster of visual field maps, but demonstrated dynamic changes across the lifespan. These data would suggest that gradient 2 tracks the functional differentiation of visual cortex into unique regions, wherein regions occupying the same hierarchical level within gradient 1 show distinct values in gradient 2. Given that gradient 2 shows the strongest relationship to behavior and tracks developmental changes across the lifespan, it might suggest that developmental differentiation between cortical regions during childhood more strongly drives maturation of visual behavior, compared to global structural changes. Future work can examine if functional arealization at earlier developmental timepoints, as in infancy[62], follows this prediction. Likewise, as regions become architecturally similar in later adulthood and less differentiated compared to young adulthood, visual behavioral performance decreases. The extent to which these architectural changes reflect local tissue structure versus connectomic features[63] can be clarified in future work. These findings offer evidence that there are architectural gradients, measurable with MRI, that are shared across individuals. These shared patterns of cortical sheet morphology track the functional organization and computations of the underlying cortical sheet across the human lifespan. These findings provide a normative benchmark for future work examining how deviations from these shared mesoscale architectural patterns underlie neurological disorders.

## Methods

### Human Connectome Project Data

The publicly-available data from the HCP Young Adult (HCP-YA)[20,22], Development (HCP-D) and Aging (HCP-A)[60] were used in the study. The three large-scale brain imaging

bioRxiv preprint doi: https://doi.org/10.1101/2023.11.29.569190; this version posted November 30, 2023. The copyright holder for this preprint (which was not certified by peer review) is the author/funder, who has granted bioRxiv a license to display the preprint in perpetuity. It is made available under aCC-BY-NC-ND 4.0 International license.

studies collect behavioral and multi-modal MRI data in healthy participants from 5 to 100 years of age, and thus provide us with opportunities to characterize brain changes across the human lifespans. Only structural MRI, resting-state fMRI and behavioral data were used in the study. The use and analyses were approved by the Institutional Review Boards of Beijing Normal University and Princeton University.

After excluding participants with invalid MSM-All registration and those without any resting-state functional MRI (rs-fMRI) data, we obtained multi-modal MRI and behavioral data for 1070 HCP-YA participants (586 females, ages 22-37, S1200 release). For each participant, T1-weighted (T1w) and T2-weighted (T2w) structural images (0.7mm isotropic voxels) and functional images (2mm isotropic voxels; TR=720ms) were acquired on the HCP's customized 3-Tesla Siemens Skyra scanner using a 32-channel head coil. The rs-fMRI paradigm included two sessions, each session itself including two runs with opposite phase-encoding directions (R/L and L/R, each 15 minutes long). All the structural and functional MRI data were preprocessed using the HCP minimal preprocessing pipelines, and more information regarding data acquisition and preprocessing is available from previous work[22,64,65].

The HCP-D and HCP-A datasets were acquired on a 3T Siemens Prisma scanner with similar protocol as the HCP-YA data[19,21]. Structural MRI data (0.8mm isotropic) from 652 HCP-D participants (351 females, ages 5-21) and 725 HCP-A participants (406 females, ages 36-100) were used in this study (Lifespan HCP release 2.0). Preprocessing of these two datasets was nearly identical to that of the HCP-YA with small adaptations to account for the variability of the wider age range[60]. The HCP data used in this study were in fsLR_32k cortical space based on the MSM-All registration[66], and cortical thickness data used in the study have been regressed out to exclude the linear effect of cortical curvature.

BigBrain Data

The BigBrain dataset is a volumetric reconstruction (20 μm isotropic) of a histologically processed postmortem brain of a human male 65 years of age. Sections were stained for cell bodies, imaged, and digitally reconstructed into 3D volume[53]. The white and pial surfaces of the BigBrain were extracted at the gray-white matter boundary and gray matter/cerebrospinal fluid (CSF) boundary[67], respectively. The 3D laminar atlas, including six cortical layers, was also derived at 20 μm isotropic resolution[67,68]. Based on the surface registration to the MRI-based MNI152 template surface, the cytoarchitectural information from each layer of the BigBrain can be linked to in vivo neuroimaging data.

Population receptive field (pRF) experiment

We performed pRF mapping on 12 participants with high-contrast, ecological images to better drive neurons of high-level visual cortex often tuned for such complex objects. We adapted the experiment used in the HCP 7T Retinotopy Dataset[45]. Stimuli consisted of slowly-moving bar-shaped apertures of 2-degree width filled with a dynamic colorful texture. Textures presented within the bar aperture were updated at a rate of 7 Hz. Textures included randomly-

bioRxiv preprint doi: https://doi.org/10.1101/2023.11.29.569190; this version posted November 30, 2023. The copyright holder for this preprint (which was not certified by peer review) is the author/funder, who has granted bioRxiv a license to display the preprint in perpetuity. It is made available under aCC-BY-NC-ND 4.0 International license.

presented cartoon scenes depicting people, animals, characters, text, limbs and objects evenly spanning the width of the stimulus aperture. Participants were asked to fixate on a central dot while attending to the bar, monitoring it for the random appearance of a target cartoon stimulus (a grid of wiggling bumblebees) which appeared for a 500ms duration, 10 times during the experiment. Each run lasted 300s, and participants completed 3 to 4 runs.

Data Analysis

*Definition of human visual cortex.* Human visual cortex was defined by grouping the 44 visual areas from the HCP multimodal parcellation (MMP) atlas[8]. All of these areas located in the occipital, parietal and temporal cortices and show a significant BOLD response to visual objects. According to the well-established model of the visual cortex, these areas are grouped into four visual processing streams: early stream (V1, V2, V3, V4), lateral stream (V3CD, LO1, LO2, LO3, V4t, FST, MT, MST, PH); dorsal (V3A, V3B, V6, V6A, V7, IPS1, LIPv, VIP, MIP, 7Am, 7PL, 7Pm, IP0, IP1, DVT, ProS, POS1, POS2, PCV), and ventral (V8, VVC, PIT, FFC, VMV1, VMV2, VMV3, PeEc, PHA1, PHA2, PHA3, TF). Please see supplementary information for the detailed descriptions of these areas (Table 1).

*Extracting architectural gradients of human visual cortex.* Cortical thickness and cortical myelin content, the two widely used mesoscale in-vivo architectural measures derived from structural MRI were used to extract architectural gradients of human visual cortex. Cortical thickness was measured as the shortest distance between each vertex on the white matter surface and the pial surface[23], while cortical myelin content was measured by the ratio of T1w to T2w[24]. For each of hemisphere, individual cortical thickness and myelin content maps from all HCP-YA participants were concatenated and a principal component analysis (PCA)[39] was conducted to linearly decompose the concatenated maps into a collection of orthogonal principal components (PCs), consisting of spatial maps (i.e., score) and individual weights (i.e., loading) in pairs. The score map explains how the structural properties change across the cortical sheet on each component and the individual weights describe how individual cortical thickness and myelin content maps contributes to each component. The PCs are sorted in decreasing order according to the amount of variance explained by each of the component. The contribution ratio of myelination or thickness for a given PC was calculated by the ratio of the sum of absolute values of weights of the loading matrix from each measure to the sum of absolute values of weights from both measures.

*The global hierarchy of the architectural gradients.* Two metrics which index the visual cortical functional hierarchy were used to validate the global hierarchy of the architectural gradients.

(1) Population receptive field (pRF) size: It is widely known that pRF size progressively increases as one ascends the processing hierarchy from V1 to high-level visual cortex[15,46,47]. We first validated the global hierarchy of the architectural gradients by measuring if the

bioRxiv preprint doi: https://doi.org/10.1101/2023.11.29.569190; this version posted November 30, 2023. The copyright holder for this preprint (which was not certified by peer review) is the author/funder, who has granted bioRxiv a license to display the preprint in perpetuity. It is made available under aCC-BY-NC-ND 4.0 International license.

gradients show similar spatial pattern to the pRF size across visual areas. Specifically, we calculated the Pearson correlation coefficients between architectural gradients and pRF size from the HCP's 7T retinotopy dataset[45]. Only the vertices whose eccentricity of pRF within 8 degrees were used because retinotopic mapping stimuli were constrained to a circular region with a radius of 8 degrees.

(2) Hierarchical rank: As the hierarchical level of the visual areas within the ventral stream has been widely studied and relatively clear, we reviewed literature describing the hierarchical relationships of 10 visual areas within the ventral stream[7,8,69–82] and ranked them into a hierarchy from lowest-level to high: V1, V2, V3, V4, V8, PIT, VVC, FFC, TF, and PeEc, with cortical regions defined using labels of the HCP multimodal atlas[8]. Spearman's rank correlation coefficients were then computed between the mean gradient score and the hierarchical rank of the areas.

*Geometric models of the architectural gradients.* The geometric models of the architectural gradients were constructed by the geodesic distance of each vertex to a set of specific references (Fig. 1g). The primary gradient was modeled as the geodesic distance of each vertex of visual cortex to the calcarine sulcus (CS) anchor. The secondary gradient was modeled as the minimum geodesic distance from each vertex on the visual cortex to the eight anchors dispersed among four visual processing streams, which consisted of two local minima in the early visual cortex, two local minima in the dorsal visual stream, two local minima in the lateral visual stream, and two local minima in the ventral visual stream (Please see supplementary information for details, Table 2).

*The gradient differences between vertices with different spatial distance*. The gradient differences for each pair of vertices were calculated as the absolute difference between their gradient scores. The spatial distance between each pair of vertices was measured by the geodesic distance separating them on the cortical surface. The gradient differences between pairs of vertices were then sorted into 100 groups according to their spatial distance. The mean gradient differences and geodesic distances were then computed for each group and plotted against each other to evaluate how the gradient differences depend on spatial distance.

*Functional significance of the architectural gradients*. We characterized the functional significance of the architectural gradients by measuring to what extent each gradient is related to areal differentiation of the visual cortex[8] and the fractional amplitude of low-frequency fluctuation (fALFF) from resting-state fMRI[51].

(1) Predicting visual areas based on the architectural gradients: Logistic Regression classifiers were trained on the architectural gradients to predict visual cortical areas. Specifically, the vertices from the visual cortex, with the architectural gradients as features, were used as the samples and the 44 visual cortical areas from the HCP MMP were used as the true class labels (i.e., 44-class classification). The areas with more vertices were down sampled to have

bioRxiv preprint doi: https://doi.org/10.1101/2023.11.29.569190; this version posted November 30, 2023. The copyright holder for this preprint (which was not certified by peer review) is the author/funder, who has granted bioRxiv a license to display the preprint in perpetuity. It is made available under aCC-BY-NC-ND 4.0 International license.

the same number of vertices as the smallest areas to keep the number of samples with each class constant and thus avoid the imbalance of sample number across different visual areas. Logistic Regression classifiers were trained and tested on each downsampled data using a 5-fold cross-validation (CV) procedure. 100 random downsamples were performed and the averaged accuracy was used to measure the classification accuracy.

(2) Predicting fALFF based on the architectural gradients: The fALFF is calculated as the ratio of the power spectrum of low-frequency modulations to that of the entire frequency range and is indicative of the magnitude of spontaneous brain activity[49,51]. For each rs-fMRI run, the time series of each vertex was Fourier transformed to a frequency domain without band-pass filtering, and the square root of the power was calculated at each frequency within the spectrum. fALFF was then computed by dividing the sum of amplitudes across a low-frequency band of the spectrum (0.01–0.1 Hz) by the sum of amplitudes across all frequencies up to the Nyquist frequency (0–0.625 Hz). The group fALFF map was calculated by averaging individual fALFF across all valid rfMRI runs within each participant and then across participants. 100 linear regression analyses using the 5-fold CV procedure were performed and the averaged $R^2$ was used to characterize to what extent the two architectural gradients are related to spontaneous functional activity characterized by fALFF.

*Laminar cytoarchitecture underlying the architectural gradients*. The BigBrain cortical surfaces registered to standard surfaces, the surfaces of borders of the six cortical layers in BigBrain histological space, and the cell body density (CBD) data at 40-μm resolution were used together to extract laminar cytoarchitecture of the visual cortex. Specifically, for each of six cortical layers[67], we first generated 10 surfaces based on the equivolumetric principle between its inner and outer borders[83] to extract 10 CBD maps in the BigBrain space. Next, the CBD data from the BigBrain space were resampled to the fsLR_32k space, and then the 10 CBD maps were averaged to obtain an averaged CBD map for the layer. Finally, the spatial similarity between the architectural gradients and the averaged CBD map from each of the 6 cortical layers was measured with Pearson correlation coefficients.

*Population receptive field (pRF) mapping*. Functional images were preprocessed using a similar pipeline to the HCP data, including motion-correction, slice-timing correction, and phase-encoding distortion correction, and then aligned to each participant's native cortical surface through FreeSurfer's FS-FAST pipeline[84]. The preprocessed data from multiple runs from each participant were averaged to increase signal-to-noise ratio. The data were finally analyzed by a pRF model implemented in the VISTA Lab toolbox (github.com/vistalab), with additions for compressive nonlinearity (cvnlab.net/analyzePRF). The model predicts fMRI time series as the convolution of the stimulus-related time series and a canonical hemodynamic response function. The stimulus-related time series are in turn generated by computing the dot product between the stimulus apertures and a 2D isotropic Gaussian, scaling and applying a static power-law

bioRxiv preprint doi: https://doi.org/10.1101/2023.11.29.569190; this version posted November 30, 2023. The copyright holder for this preprint (which was not certified by peer review) is the author/funder, who has granted bioRxiv a license to display the preprint in perpetuity. It is made available under aCC-BY-NC-ND 4.0 International license.

nonlinearity[85]. Several parameters of interest are produced from the pRF model for each vertex including phase angle, eccentricity, and pRF size. Vertices entered into any analyses presented in Figure 2 were only included if there was at least 10% variance-explained by the model-fit.

*Behavioral relevance of the architectural gradients*. The behavioral significance of the architectural gradients was examined by measuring how the individual weights from PCA can account for the individual variation in behavioral performance on related visual tasks. The HCP-YA dataset include behavioral tasks of a range of motor, sensory, cognitive, and emotional processes. Because our architectural gradients cover the entire visual cortex and may involve into a variety of cognitive and behavioral abilities, a total of 15 vision-related or vision-based behavioral tasks[58], designed to measure nonverbal episodic memory ability, cognitive flexibility, inhibitory control and attention ability, fluid intelligence, reading decoding skill, general vocabulary knowledge, speed of processing, spatial orientation processing ability, sensitivity of sustained attention, specificity of sustained attention, verbal episodic memory ability, working memory ability, odor identification ability, visual acuity, and contrast sensitivity, were selected to examine the behavioral relevance of the gradients (Please see supplementary information for details, Table 3).

For the two sets of individual weights (i.e., myelin content weights and cortical thickness weights) associated with each of architectural gradient, we carried out a single integrated multivariate analysis using canonical correlation analysis (CCA)[57], to simultaneously co-analyze the two sets of gradients along with 15 behavioral variables from all participants. CCA aims to identify symmetric linear relations between the two sets of variables. That is, we used CCA to find components that relate the two sets of weights from each gradient to 15 sets of participants' behavioral measures. Each CCA component identifies a linear combination of two weights and a linear combination of behavioral variables, where the variation in strength of involvement across participants is maximally correlated. The normalized magnitude of behavioral weights was used to characterize the behavioral profile of an architectural gradient and reveal how the two gradients are different in predicting the same set of behavioral variables.

*The development of the architectural gradients across the lifespan*. We divided HCP-D, HCP-YA, and HCP-A participants into different age windows (subgroups) in ascending order of age. Among them, the participants of HCP-D and HCP-A were sorted by their age in months, while HCP-YA sorted in years because no month information was provided. Each window consisted of 50 participants and had a step size of ten. As a result, there are 61, 103, and 68 age windows generated for HCP-D, HCP-YA, and HCP-A data, respectively. To characterize the changes of the architectural gradients across the human lifespan, we conducted PCA on the stacked myelination and thickness maps of each window as we did in the whole HCP-YA data. We label the principal components from each age window as lifespan components (LC) to differentiate them from the original PCs derived from the HCP-YA dataset. To determine if the observed LCs were similar to the PCs from the HCP-YA data, we calculated the Pearson's

bioRxiv preprint doi: https://doi.org/10.1101/2023.11.29.569190; this version posted November 30, 2023. The copyright holder for this preprint (which was not certified by peer review) is the author/funder, who has granted bioRxiv a license to display the preprint in perpetuity. It is made available under aCC-BY-NC-ND 4.0 International license.

correlation coefficients between the HCP-YA PCs and the top ten LCs for each window. The LC which shows strongest correlation with a PC was considered to be the correspondence LC to the PC in that age window. Lastly, how the observed gradients from each age window change relative to the gradient from the HCP-YA was measured by the Pearson's correlation coefficient between their score maps. The changes along age were then charted (i.e., developmental trajectories). A linear model was then constructed to characterize the developmental trajectory within each of three datasets. The slope of the linear model was defined as the annualized rate of change (AROC) in the architectural gradients.

## Ethical Compliance

Data analyzed from the Human Connectome Project follows all necessary privacy and security guidelines. Data collected from participants at Princeton University followed all Institutional Review Board ethics and guidelines (protocol number 13074), and all safety regulations set forth by the Scully Center for the Neuroscience of Mind and Behavior. Informed consent was collected from every participant involved in this study, and all were reimbursed for their time.

## Data Availability

The data from the HCP Young Adult (HCP-YA) are publicly available at the https://www.humanconnectome.org; The data from the HCP Development (HCP-D) and HCP Aging (HCP-A) are publicly available at https://nda.nih.gov. Users can access these after registration.

## Code Availability

The HCP data were preprocessed using the HCP-Pipeline analyses (https://github.com/Washington-University/HCPpipelines). Custom code for gradient analysis can be found at https://github.com/BNUCNL/VisualCortexGradient. Code to reproduce population receptive field mapping figures can be found at: https://github.com/gomezj/entorhinal_prf.

## Acknowledgements

We thank Youyi Liu and the Brain Development Lab for several useful discussions. This research was supported by Child Brain-Mind Development Cohort Study in the China Brain Initiative (2021ZD0200534) and the National Natural Science Foundation of China (31771251) to ZZ. This research was supported by start-up funds from the Princeton Neuroscience Institute to JG.

## Author Contributions

JG and ZZ conceived of the idea and design of the study. XC and XL compiled the data, performed the analyses, and prepared visualizations. PH, ED, and JY performed the analyses.

bioRxiv preprint doi: https://doi.org/10.1101/2023.11.29.569190; this version posted November 30, 2023. The copyright holder for this preprint (which was not certified by peer review) is the author/funder, who has granted bioRxiv a license to display the preprint in perpetuity. It is made available under aCC-BY-NC-ND 4.0 International license.

JG, XC, XL, and ZZ drafted and revised the manuscript with input from all authors. JG and ZZ supervised the research.

## Competing Interests Statement

The authors declare no competing interests.

bioRxiv preprint doi: https://doi.org/10.1101/2023.11.29.569190; this version posted November 30, 2023. The copyright holder for this preprint (which was not certified by peer review) is the author/funder, who has granted bioRxiv a license to display the preprint in perpetuity. It is made available under aCC-BY-NC-ND 4.0 International license.

## References


1. Vergleichende Lokalisationslehre der Großhirnrinde : in ihren Prinzipien dargestellt auf Grund des Zellenbaues / von K. Brodmann. (1909).
2. Brodmann, K. & Gary, L. J. Brodmann's localisation in the cerebral cortex: the principles of comparative localisation in the cerebral cortex based on cytoarchitectonics. (Springer, 2006).
3. Vogt, C. & Vogt, O. Allgemeine ergebnisse unserer hirnforschung. vol. 25 (JA Barth, 1919).
4. Amunts, K. & Zilles, K. Architectonic Mapping of the Human Brain beyond Brodmann. Neuron **88**, 1086–1107 (2015).
5. Amunts, K., Mohlberg, H., Bludau, S. & Zilles, K. Julich-Brain: A 3D probabilistic atlas of the human brain's cytoarchitecture. Science **369**, 988–992 (2020).
6. Burt, J. B. et al. Hierarchy of transcriptomic specialization across human cortex captured by structural neuroimaging topography. Nat. Neurosci. **21**, 1251–1259 (2018).
7. Gomez, J., Zhen, Z. & Weiner, K. S. Human visual cortex is organized along two genetically opposed hierarchical gradients with unique developmental and evolutionary origins. PLOS Biol. **17**, e3000362 (2019).
8. Glasser, M. F. et al. A multi-modal parcellation of human cerebral cortex. Nature **536**, 171–178 (2016).
9. Lerch, J. P. et al. Studying neuroanatomy using MRI. Nat. Neurosci. **20**, 314–326 (2017).
10. Sebenius, I. et al. Robust estimation of cortical similarity networks from brain MRI. Nat. Neurosci. **26**, 1461–1471 (2023).
11. Genon, S., Eickhoff, S. B. & Kharabian, S. Linking interindividual variability in brain structure to behaviour. Nat. Rev. Neurosci. **23**, 307–318 (2022).
12. Miller, J. A., Voorhies, W. I., Lurie, D. J., D'Esposito, M. & Weiner, K. S. Overlooked Tertiary Sulci Serve as a Meso-Scale Link between Microstructural and Functional Properties of Human Lateral Prefrontal Cortex. J. Neurosci. Off. J. Soc. Neurosci. **41**, 2229–2244 (2021).
13. Grotheer, M. et al. White matter myelination during early infancy is linked to spatial gradients and myelin content at birth. Nat. Commun. **13**, 997 (2022).
14. Sowell, E. R. et al. Longitudinal Mapping of Cortical Thickness and Brain Growth in Normal Children. J. Neurosci. **24**, 8223–8231 (2004).
15. Wandell, B. A. & Winawer, J. Computational neuroimaging and population receptive fields. Trends Cogn. Sci. **19**, 349–357 (2015).
16. Gomez, J., Natu, V., Jeska, B., Barnett, M. & Grill-Spector, K. Development differentially sculpts receptive fields across early and high-level human visual cortex. Nat. Commun. **9**, 788 (2018).
17. Stigliani, A., Weiner, K. S. & Grill-Spector, K. Temporal Processing Capacity in High-Level Visual Cortex Is Domain Specific. J. Neurosci. Off. J. Soc. Neurosci. **35**, 12412–12424 (2015).
18. Hasson, U., Yang, E., Vallines, I., Heeger, D. J. & Rubin, N. A hierarchy of temporal receptive windows in human cortex. J. Neurosci. **28**, 2539–2550 (2008).

bioRxiv preprint doi: https://doi.org/10.1101/2023.11.29.569190; this version posted November 30, 2023. The copyright holder for this preprint (which was not certified by peer review) is the author/funder, who has granted bioRxiv a license to display the preprint in perpetuity. It is made available under aCC-BY-NC-ND 4.0 International license.

19. Bookheimer, S. Y. et al. The Lifespan Human Connectome Project in Aging: An overview. NeuroImage **185**, 335–348 (2019).
20. Van Essen, D. C. et al. The WU-Minn Human Connectome Project: An overview. NeuroImage **80**, 62–79 (2013).
21. Somerville, L. H. et al. The Lifespan Human Connectome Project in Development: A large-scale study of brain connectivity development in 5-21 year olds. NeuroImage **183**, 456–468 (2018).
22. Glasser, M. F. et al. The minimal preprocessing pipelines for the Human Connectome Project. NeuroImage **80**, 105–124 (2013).
23. Fischl, B. & Dale, A. M. Measuring the thickness of the human cerebral cortex from magnetic resonance images. Proc. Natl. Acad. Sci. U. S. A. **97**, 11050–11055 (2000).
24. Glasser, M. F. & Essen, D. C. V. Mapping Human Cortical Areas In Vivo Based on Myelin Content as Revealed by T1- and T2-Weighted MRI. J. Neurosci. **31**, 11597–11616 (2011).
25. Carlo, C. N. & Stevens, C. F. Structural uniformity of neocortex, revisited. Proc. Natl. Acad. Sci. U. S. A. **110**, 1488–1493 (2013).
26. Huttenlocher, P. R. & Dabholkar, A. S. Regional differences in synaptogenesis in human cerebral cortex. J. Comp. Neurol. **387**, 167–178 (1997).
27. Natu, V. S. et al. Apparent thinning of human visual cortex during childhood is associated with myelination. Proc. Natl. Acad. Sci. **116**, 20750–20759 (2019).
28. Bo, T. et al. Brain-wide and cell-specific transcriptomic insights into MRI-derived cortical morphology in macaque monkeys. Nat. Commun. **14**, 1499 (2023).
29. Preziosa, P. et al. Neurite density explains cortical T1-weighted/T2-weighted ratio in multiple sclerosis. J. Neurol. Neurosurg. Psychiatry **92**, 790–792 (2021).
30. Grill-Spector, K. & Weiner, K. S. The functional architecture of the ventral temporal cortex and its role in categorization. Nat. Rev. Neurosci. **15**, 536–548 (2014).
31. Witthoft, N. et al. Where is human V4? Predicting the location of hV4 and VO1 from cortical folding. Cereb. Cortex N. Y. N 1991 **24**, 2401–2408 (2014).
32. Dumoulin, S. O. et al. A new anatomical landmark for reliable identification of human area V5/MT: a quantitative analysis of sulcal patterning. Cereb. Cortex N. Y. N 1991 **10**, 454–463 (2000).
33. Gomez, J. et al. Development of population receptive fields in the lateral visual stream improves spatial coding amid stable structural-functional coupling. NeuroImage **188**, 59–69 (2019).
34. Konkle, T. & Caramazza, A. Tripartite organization of the ventral stream by animacy and object size. J. Neurosci. Off. J. Soc. Neurosci. **33**, 10235–10242 (2013).
35. Wandell, B. A. & Winawer, J. Imaging retinotopic maps in the human brain. Vision Res. **51**, 718–737 (2011).
36. Benson, N. C. & Winawer, J. Bayesian analysis of retinotopic maps. eLife **7**, e40224 (2018).

bioRxiv preprint doi: https://doi.org/10.1101/2023.11.29.569190; this version posted November 30, 2023. The copyright holder for this preprint (which was not certified by peer review) is the author/funder, who has granted bioRxiv a license to display the preprint in perpetuity. It is made available under aCC-BY-NC-ND 4.0 International license.


37. Konen, C. S. & Kastner, S. Representation of eye movements and stimulus motion in topographically organized areas of human posterior parietal cortex. J. Neurosci. Off. J. Soc. Neurosci. **28**, 8361–8375 (2008).
38. Hong, S.-J. et al. Toward a connectivity gradient-based framework for reproducible biomarker discovery. NeuroImage **223**, 117322 (2020).
39. Lever, J., Krzywinski, M. & Altman, N. Principal component analysis. Nature Methods vol. 14 641–642 https://www.nature.com/articles/nmeth.4346 (2017).
40. Wandell, B. A., Dumoulin, S. O. & Brewer, A. A. Visual Field Maps in Human Cortex. Neuron **56**, 366–383 (2007).
41. Pitcher, D. & Ungerleider, L. G. Evidence for a Third Visual Pathway Specialized for Social Perception. Trends Cogn. Sci. **25**, 100–110 (2021).
42. Weiner, K. S. & Gomez, J. Third Visual Pathway, Anatomy, and Cognition across Species. Trends Cogn. Sci. **25**, 548–549 (2021).
43. Ungerleider, L. G. & Haxby, J. V. 'What' and 'where' in the human brain. Curr. Opin. Neurobiol. **4**, 157–165 (1994).
44. Goodale, M. A. & Milner, A. D. Separate visual pathways for perception and action. Trends Neurosci. **15**, 20–25 (1992).
45. Benson, N. C. et al. The Human Connectome Project 7 Tesla retinotopy dataset: Description and population receptive field analysis. J. Vis. **18**, 23 (2018).
46. Dumoulin, S. O. & Wandell, B. A. Population receptive field estimates in human visual cortex. NeuroImage **39**, 647–660 (2008).
47. Amano, K., Wandell, B. A. & Dumoulin, S. O. Visual field maps, population receptive field sizes, and visual field coverage in the human MT+ complex. J. Neurophysiol. **102**, 2704–2718 (2009).
48. Harvey, B. M. & Dumoulin, S. O. The relationship between cortical magnification factor and population receptive field size in human visual cortex: constancies in cortical architecture. J. Neurosci. Off. J. Soc. Neurosci. **31**, 13604–13612 (2011).
49. Shmuel, A. & Leopold, D. A. Neuronal correlates of spontaneous fluctuations in fMRI signals in monkey visual cortex: Implications for functional connectivity at rest. Hum. Brain Mapp. **29**, 751–761 (2008).
50. Sydnor, V. J. et al. Intrinsic activity development unfolds along a sensorimotor-association cortical axis in youth. Nat. Neurosci. **26**, 638–649 (2023).
51. Zou, Q.-H. et al. An improved approach to detection of amplitude of low-frequency fluctuation (ALFF) for resting-state fMRI: fractional ALFF. J. Neurosci. Methods **172**, 137–141 (2008).
52. Stigliani, A., Jeska, B. & Grill-Spector, K. Encoding model of temporal processing in human visual cortex. Proc. Natl. Acad. Sci. U. S. A. **114**, E11047–E11056 (2017).
53. Amunts, K. et al. BigBrain: An Ultrahigh-Resolution 3D Human Brain Model. Science **340**, 1472–1475 (2013).

bioRxiv preprint doi: https://doi.org/10.1101/2023.11.29.569190; this version posted November 30, 2023. The copyright holder for this preprint (which was not certified by peer review) is the author/funder, who has granted bioRxiv a license to display the preprint in perpetuity. It is made available under aCC-BY-NC-ND 4.0 International license.

54. Brewer, A. A., Liu, J., Wade, A. R. & Wandell, B. A. Visual field maps and stimulus selectivity in human ventral occipital cortex. Nat. Neurosci. **8**, 1102–1109 (2005).
55. Finzi, D. et al. Differential spatial computations in ventral and lateral face-selective regions are scaffolded by structural connections. Nat. Commun. **12**, 2278 (2021).
56. Axelrod, V. & Yovel, G. The challenge of localizing the anterior temporal face area: a possible solution. NeuroImage **81**, 371–380 (2013).
57. Wang, H.-T. et al. Finding the needle in a high-dimensional haystack: Canonical correlation analysis for neuroscientists. NeuroImage **216**, 116745 (2020).
58. Barch, D. M. et al. Function in the human connectome: task-fMRI and individual differences in behavior. NeuroImage **80**, 169–189 (2013).
59. Gomez, J. et al. Microstructural proliferation in human cortex is coupled with the development of face processing. Science **355**, 68–71 (2017).
60. Harms, M. P. et al. Extending the Human Connectome Project across ages: Imaging protocols for the Lifespan Development and Aging projects. NeuroImage **183**, 972–984 (2018).
61. Yeatman, J. D., Wandell, B. A. & Mezer, A. A. Lifespan maturation and degeneration of human brain white matter. Nat. Commun. **5**, 4932 (2014).
62. Wang, F. et al. Fine-grained functional parcellation maps of the infant cerebral cortex. eLife **12**, e75401 (2023).
63. Sarwar, T., Tian, Y., Yeo, B. T. T., Ramamohanarao, K. & Zalesky, A. Structure-function coupling in the human connectome: A machine learning approach. NeuroImage **226**, 117609 (2021).
64. Van Essen, D. C. et al. The Human Connectome Project: a data acquisition perspective. NeuroImage **62**, 2222–2231 (2012).
65. Glasser, M. F. et al. The Human Connectome Project's neuroimaging approach. Nat. Neurosci. **19**, 1175–1187 (2016).
66. Robinson, E. C. et al. Multimodal surface matching with higher-order smoothness constraints. NeuroImage **167**, 453–465 (2018).
67. Wagstyl, K. et al. Mapping Cortical Laminar Structure in the 3D BigBrain. Cereb. Cortex N. Y. N 1991 **28**, 2551–2562 (2018).
68. Wagstyl, K. et al. BigBrain 3D atlas of cortical layers: Cortical and laminar thickness gradients diverge in sensory and motor cortices. PLoS Biol. **18**, e3000678 (2020).
69. Abdollahi, R. O. et al. Correspondences between retinotopic areas and myelin maps in human visual cortex. NeuroImage **99**, 509–524 (2014).
70. Beauchamp, M. S., Yasar, N. E., Frye, R. E. & Ro, T. Touch, sound and vision in human superior temporal sulcus. NeuroImage **41**, 1011–1020 (2008).
71. Felleman, D. J. & Van Essen, D. C. Distributed Hierarchical Processing in the Primate Cerebral Cortex. Cereb. Cortex **1**, 1–47 (1991).
72. Hadjikhani, N., Liu, A. K., Dale, A. M., Cavanagh, P. & Tootell, R. B. Retinotopy and color sensitivity in human visual cortical area V8. Nat. Neurosci. **1**, 235–241 (1998).

bioRxiv preprint doi: https://doi.org/10.1101/2023.11.29.569190; this version posted November 30, 2023. The copyright holder for this preprint (which was not certified by peer review) is the author/funder, who has granted bioRxiv a license to display the preprint in perpetuity. It is made available under aCC-BY-NC-ND 4.0 International license.

73. Haxby, J. V., Hoffman, E. A. & Gobbini, M. I. The distributed human neural system for face perception. Trends Cogn. Sci. **4**, 223–233 (2000).
74. Kolster, H., Peeters, R. & Orban, G. A. The retinotopic organization of the human middle temporal area MT/V5 and its cortical neighbors. J. Neurosci. Off. J. Soc. Neurosci. **30**, 9801–9820 (2010).
75. Larsson, J. & Heeger, D. J. Two retinotopic visual areas in human lateral occipital cortex. J. Neurosci. Off. J. Soc. Neurosci. **26**, 13128–13142 (2006).
76. Moreno-Ortega, M. et al. Resting state functional connectivity predictors of treatment response to electroconvulsive therapy in depression. Sci. Rep. **9**, 5071 (2019).
77. Nunn, J. A. et al. Functional magnetic resonance imaging of synesthesia: activation of V4/V8 by spoken words. Nat. Neurosci. **5**, 371–375 (2002).
78. Orban, G. A., Van Essen, D. & Vanduffel, W. Comparative mapping of higher visual areas in monkeys and humans. Trends Cogn. Sci. **8**, 315–324 (2004).
79. Sellal, F. Anatomical and neurophysiological basis of face recognition. Rev. Neurol. (Paris) **178**, 649–653 (2022).
80. Tootell, R. B. et al. Functional analysis of V3A and related areas in human visual cortex. J. Neurosci. Off. J. Soc. Neurosci. **17**, 7060–7078 (1997).
81. Tootell, R. B. H., Tsao, D. & Vanduffel, W. Neuroimaging Weighs In: Humans Meet Macaques in “Primate” Visual Cortex. J. Neurosci. **23**, 3981–3989 (2003).
82. Weiner, K. S. et al. The mid-fusiform sulcus: A landmark identifying both cytoarchitectonic and functional divisions of human ventral temporal cortex. NeuroImage **84**, 453–465 (2014).
83. Waehnert, M. D. et al. Anatomically motivated modeling of cortical laminae. NeuroImage **93 Pt 2**, 210–220 (2014).
84. Fischl, B. FreeSurfer. NeuroImage **62**, 774–781 (2012).
85. Kay, K. N., Winawer, J., Mezer, A. & Wandell, B. A. Compressive spatial summation in human visual cortex. J. Neurophysiol. **110**, 481–494 (2013).